Available online at www.sciencedirect.com
ScienceDirect
International Journal of Thermal Sciences 46 (2007) 458–466
International Journal of Thermal Sciences
www.elsevier.com/locate/ijts

Two-phase modelling of laminar film condensation from vapour–gas mixtures in declining parallel-plate channels

E.C. Siow, S.J. Ormiston *, H.M. Soliman

Department of Mechanical and Manufacturing Engineering, University of Manitoba, 75A Chancellors Circle, Winnipeg, Manitoba, R3T 5V6, Canada

Received 25 December 2005; accepted 2 July 2006

Available online 1 August 2006

Abstract

A two-phase model is presented that analyzes laminar film condensation from mixtures of a vapour and a non-condensing gas in parallel-plate channels. The channel is declining (inclined downward from the horizontal) and has an isothermal cooled bottom plate and an insulated upper plate. The model uses a finite volume method to solve the complete two-phase boundary-layer equations including inertia forces, energy convection, interfacial shear, and axial pressure change. Results are presented for steam–air mixtures in terms of axial variation of film thickness and local Nusselt number for various Froude numbers, inlet Reynolds numbers, inlet gas mass fractions, and inlet temperature differences. Profiles of axial velocity, temperature, and gas mass fraction are also presented. Increasing the angle of declination (decreasing the Froude number) produces thinner, faster moving films. The change in local Nusselt number with Froude number was not as substantial as the change in film thickness. The detrimental effect of the noncondensable gas on the heat transfer rate was observed to be more pronounced at higher Froude numbers. An exact analytical solution for the liquid and mixture axial velocity profiles under end of condensation conditions is also presented and compared with the numerical results.

Keywords: Film condensation; Laminar; Noncondensable gas; Two-phase model

1. Introduction

Film condensation in ducts is a process that is pertinent to system components in the power, refrigeration, air-conditioning, and chemical industries. Consequently, numerous previous experimental and theoretical studies have been made aimed at improving the understanding of the condensation process for various duct geometries, duct orientations, and fluid properties. For condensation in a channel formed by two parallel plates, a number of detailed numerical studies of film condensation have been reported. In the horizontal orientation, Louahlia and Panday [1,2], and Narain and Kizilyalli [3] performed studies of condensation from pure vapours and Siow et al. [4] included the effect of a non-condensing gas. In the vertical orientation, Louahlia and Panday [5,6] studied pure vapours and Siow et al. [7] studied steam–air mixtures. In the case of the declining (i.e., downward-inclined) orientation, the work of Narain et al. [8] was concerned with condensation from pure vapours while Siow et al. [9] reported preliminary results for steam–air mixtures.

To the authors' best knowledge, there are no published experimental studies on laminar film condensation from vapour–gas mixtures for declining parallel-plate channels. The only related experimental studies found are the studies of single-sided condensation in horizontal channels by Lu and Suryanarayana [10] and Yu et al. [11] and the inclined plate experiment of Chung et al. [12]. Chung et al. studied condensation on an inclined cooled plate placed in an upward flow of pure steam or steam–air mixtures. The plate was oriented at 20 or 45 degrees from the horizontal and the cooled side faced upwards and downwards.

The objective of this work is to present new modelling results for condensing flow in declining parallel-plate channels, including the effects of non-condensing gas. The results for the effect of declination are presented using a Froude number, rather than for specific angles of declination.

* Corresponding author. Tel.: +1 204 474 8639; fax: +1 204 275 7507.
E-mail address: SJ_Ormiston@UManitoba.CA (S.J. Ormiston).

1290-0729/$ – see front matter
doi:10.1016/j.ijthermalsci.2006.07.001

Nomenclature

C_p	specific heat	$\mathrm{J\,kg^{-1}\,K^{-1}}$	
D	diffusion coefficient	$\mathrm{m^2\,s^{-1}}$	
Fr	Froude number, $u_{\mathrm{in}}{}^2/(Hg\sin\theta)$		
g	gravitational acceleration	$\mathrm{m\,s^{-2}}$	
h_{fg}	latent heat of vapourisation	$\mathrm{J\,kg^{-1}}$	
H	plate spacing	m	
J''	mass flux	$\mathrm{kg\,s^{-1}\,m^{-2}}$	
k	thermal conductivity	$\mathrm{W\,m^{-1}\,K^{-1}}$	
$\dot{m}'$	mass flow rate per unit depth	$\mathrm{kg\,s^{-1}\,m^{-1}}$	
Nu_x	local Nusselt number, $(q''_{\mathrm{wall}}H)/(k_L\Delta T)$		
$\overline{Nu}_x$	average Nusselt number		
P	pressure	$\mathrm{N\,m^{-2}}$	
$P^\star$	dimensionless pressure, $(P-P_{\mathrm{in}})/(0.5\rho_{\mathrm{in}}u_{\mathrm{in}}^2)$		
q''	local wall heat flux	$\mathrm{W\,m^{-2}}$	
Re_{in}	inlet Reynolds number, $(\rho_{\mathrm{in}}u_{\mathrm{in}}H)/(\mu_{\mathrm{in}})$		
Re_δ	film Reynolds number, $(4\dot{m}'_L)/(\mu_L)$		
T	temperature	K	
$T^\star$	dimensionless temperature, $(T-T_{\mathrm{wall}})/(\Delta T)$		
u	velocity component in the x direction	$\mathrm{m\,s^{-1}}$	
$u^\star$	dimensionless x-direction velocity, (u/u_{in})		
v	velocity component in the y direction	$\mathrm{m\,s^{-1}}$	
W	gas mass fraction		
x	axial co-ordinate direction	m	
$x^\star$	dimensionless x co-ordinate, (x/H)		
y	transverse co-ordinate direction	m	
$y^\star$	dimensionless y co-ordinate, (y/H)		

Greek symbols

δ	liquid film thickness	m
$\delta^\star$	dimensionless film thickness, (δ/H)	
ΔT	inlet temperature difference, $(T_{\mathrm{in}}-T_{\mathrm{wall}})$	K
η	y-direction transformation variable	
μ	viscosity	$\mathrm{N\,s\,m^{-2}}$
ρ	density	$\mathrm{kg\,m^{-3}}$
θ	angle of declination	rad

Subscripts

ec	end of condensation
g	noncondensable gas
i	liquid–mixture interface
in	inlet
L	liquid
M	vapour–gas mixture
v	vapour
wall	lower plate

This work briefly describes a robust two-phase model for film condensation from vapour–gas mixtures. This model solves the full boundary layer equations of motion in both phases, uses a mesh that adapts to the changing film thickness, and implements fundamental mass, momentum, and energy balances at a clearly defined liquid–mixture interface. The numerical model is capable of obtaining solutions for the situation when condensation ceases after some distance down the channel and is shown to match the exact analytical solution at the end of condensation. Detailed results are presented for condensation from steam–air mixtures. Local velocity, temperature, and gas mass fraction profiles at various axial locations are used to help understand the predicted fluid flow and heat transfer behaviour. In addition, the effects of changes in the declination and inlet conditions are discussed.

2. Mathematical model

2.1. Domain definition

The domain studied is shown in Fig. 1. A mixture of vapour and non-condensable gas enters the parallel plate duct with uniform velocity, temperature, gas mass fraction, and pressure. At the inlet, the difference in temperature between the mixture and the isothermal lower plate is ΔT. The duct is declining at an angle θ from the horizontal and the gravitational acceleration acts vertically downward. Along the duct, a condensate layer forms on the cooled lower plate. Above the film is a vapour–gas region where hydrodynamic, thermal, and mass fraction boundary layers form at the liquid–mixture interface and a hydrodynamic

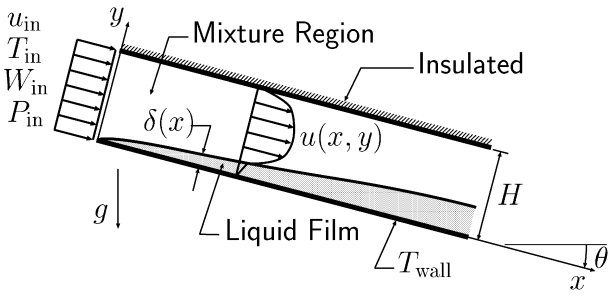

Fig. 1. Domain definition.

boundary layer forms at the upper plate. Along the duct, the removal of vapour from the mixture via condensation causes the local gas mass fraction to increase axially and reduces the bulk velocity of the mixture flow.

2.2. Governing equations

The governing equations are written for conservation of mass, momentum, and energy for each of the condensate layer and mixture regions in the duct shown in Fig. 1. It has been assumed that the flow is laminar and incompressible, that the fluids are Newtonian, that the axial diffusion terms are negligible, and that the pressure is uniform in the y direction. Thermodynamic and transport properties of the fluids are calculated at the local conditions as described in Srzic et al. [13].

In the liquid film, the equations for conservation of mass, momentum, and energy, respectively, are:

$$\frac{\partial}{\partial x}(\rho_L u_L) + \frac{\partial}{\partial y}(\rho_L v_L) = 0 \tag{1}$$

$$\frac{\partial}{\partial x}(\rho_L u_L u_L) + \frac{\partial}{\partial y}(\rho_L v_L u_L) = -\frac{\mathrm{d}P}{\mathrm{d}x} + \frac{\partial}{\partial y}\left(\mu_L \frac{\partial u_L}{\partial y}\right) + \rho_L g \sin\theta \tag{2}$$

$$\frac{\partial}{\partial x}(\rho_L u_L C_{pL} T_L) + \frac{\partial}{\partial y}(\rho_L v_L C_{pL} T_L) = \frac{\partial}{\partial y}\left(k_L \frac{\partial T_L}{\partial y}\right) \tag{3}$$

The vapour–gas mixture phase is treated as an ideal gas mixture. At the inlet to the channel and at the liquid–mixture interface, saturation conditions are assumed, so that the temperature is the equilibrium saturation temperature corresponding to the local partial pressure of the vapour. The conservation equations for mixture mass, mixture momentum, mixture energy, and gas mass, respectively, are:

$$\frac{\partial}{\partial x}(\rho_M u_M) + \frac{\partial}{\partial y}(\rho_M v_M) = 0 \tag{4}$$

$$\frac{\partial}{\partial x}(\rho_M u_M u_M) + \frac{\partial}{\partial y}(\rho_M v_M u_M) = -\frac{\mathrm{d}P}{\mathrm{d}x} + \frac{\partial}{\partial y}\left(\mu_M \frac{\partial u_M}{\partial y}\right) + \rho_M g \sin\theta \tag{5}$$

$$\frac{\partial}{\partial x}(\rho_M u_M C_{pM} T_M) + \frac{\partial}{\partial y}(\rho_M v_M C_{pM} T_M) = \frac{\partial}{\partial y}\left(k_M \frac{\partial T_M}{\partial y}\right) + \frac{\partial}{\partial y}\left(\rho_M D(C_{pg} - C_{pv})\frac{\partial W}{\partial y} T_M\right) \tag{6}$$

$$\frac{\partial}{\partial x}(\rho_M u_M W) + \frac{\partial}{\partial y}(\rho_M v_M W) = \frac{\partial}{\partial y}\left(\rho_M D \frac{\partial W}{\partial y}\right) \tag{7}$$

Equations for the boundary conditions applicable to Eqs. (1)–(7) are given below.

At the lower plate ($y = 0$):

$$u_L = v_L = 0 \tag{8}$$

$$T_L = T_{\text{wall}} \tag{9}$$

At the liquid–mixture interface ($y = \delta$):

$$u_L = u_M \tag{10}$$

$$J_i'' = \rho_L v_L - \rho_L u_L \frac{\mathrm{d}\delta}{\mathrm{d}x} = \rho_M v_M - \rho_M u_M \frac{\mathrm{d}\delta}{\mathrm{d}x} \tag{11}$$

$$T_L = T_M = T_i \tag{12}$$

$$J_i'' W - \rho_M D \frac{\partial W}{\partial y} = 0 \tag{13}$$

$$k_L \frac{\partial T_L}{\partial y} = k_M \frac{\partial T_M}{\partial y} - J_i'' h_{fg} \tag{14}$$

$$\mu_L \frac{\partial u_L}{\partial y} = \mu_M \frac{\partial u_M}{\partial y} \tag{15}$$

At the upper plate ($y = H$):

$$u_M = v_M = 0 \tag{16}$$

$$\frac{\partial T_M}{\partial y} = \frac{\partial W}{\partial y} = 0 \tag{17}$$

At the inlet u_{in}, T_{in}, W_{in}, and P_{in} are specified with uniform profiles, and the film thickness is zero.

The governing equations (Eqs. (1)–(7)) and the boundary conditions (Eqs. (8)–(17) and the inlet conditions) provide the necessary relations for determining the seven field variables u_L, v_L, T_L, u_M, v_M, T_M and W and the scalar δ. The interfacial energy balance (Eq. (14)) is used as the constraint equation for δ.

The scalar $\mathrm{d}P/\mathrm{d}x$ is also part of the set of unknowns. The constraint equation for $\mathrm{d}P/\mathrm{d}x$ is a global mass balance at any given x:

$$\int_0^{\delta} \rho_L u_L \,\mathrm{d}y + \int_{\delta}^{H} \rho_M u_M \,\mathrm{d}y = \dot{m}'_{\text{in}} \tag{18}$$

where $\dot{m}'_{\text{in}}$ is the inlet total mass flow rate per unit depth.

2.3. End of condensation

At a sufficient distance downstream from the inlet, under some operating conditions, the mixture and liquid flows reach a condition where condensation ceases. This condition arises when the mixture temperature has everywhere cooled to T_{wall} and the mixture has become a gas fully saturated with vapour. In this region, referred to here as the end of condensation, the axial velocities, the pressure gradient, and the film thickness are constant with respect to x. In this case, the momentum equations in the liquid and mixture regions are considerably simplified and can be solved analytically.

Appendix A briefly outlines the process for obtaining the end of condensation solution for the dimensionless film thickness, pressure gradient, and axial velocities.

3. Numerical solution method

Before discretization, a co-ordinate transformation was applied to the governing equations [14]. In the transformation, y was replaced by η, where

$$\eta = \frac{y}{\delta} \tag{19}$$

and

$$\eta = 1 + \left[\frac{y - \delta}{H - \delta}\right] \tag{20}$$

in the liquid and mixture regions, respectively. This transformation permitted defining the liquid–mixture interface clearly on control volume boundaries. The computational grid maintained the same number of control volumes in both phase regions all along the channel, and adapted to the changing film thickness. A uniformly spaced grid was used in the liquid region along η, and non-uniform spacing was used in the mixture region along η and along the channel in both phases. In the mixture region, the grid was contracted geometrically toward the interface and toward the upper plate. Along the channel, the grid system was expanded exponentially so that control volumes were concentrated near $x = 0$.

An algebraic analogue to Eqs. (1)–(7) was obtained using a finite volume method [15]. Upwind differencing was used in the x direction, an algebraic approximation to the exponential differencing scheme was used in the η direction, and J'' was used as a solution variable in place of v [14]. The fully coupled

solution approach used in this work is discussed by Siow et al. [4].

Solution of the linearized coupled equations was repeated at each axial station (column of control volumes) until the relative change at each node of every field and of δ and $\mathrm{d}P/\mathrm{d}x$ was less than 0.00001%. The inlet conditions or the previous station solution fields were used as the initial guess for the iterations at a given axial station. After a converged solution was obtained at any given station, the solution procedure was repeated for the next station and marched along the channel until either the prescribed channel length was reached, the film thickness reached H, or a negative axial velocity (reverse flow) was detected. The film Reynolds number (as defined in the nomenclature, with $\dot{m}'_L$ being the liquid film mass flow rate per unit depth) was also computed at all stations. For all the results presented here, the film Reynolds number at the furthest axial location shown in each case was between roughly 44 and 240. These film Reynolds numbers were judged to be sufficiently small to consider the smooth interface assumption to be reasonable.

In addition to thorough checks for conservation and consistency, the in-house computer code that implements the solution method was checked by making comparisons with a flat-plate model [16] that had been extensively compared with previous well-established laminar film analyses. In these new comparisons, the present model was run with widely spaced plates and it produced the same results as the flat-plate model near the inlet to the channel, with deviations further downstream because of the effects of the upper plate and the loss of mass due to condensation. The present model was also compared with the experiment of Lu and Suryanarayana [10] and with results of the model of Louahlia and Panday [1]. Good agreement was obtained in these comparisons [14].

For the results presented here, grid independence of the solutions was established when the total heat transfer to a channel of height 2 cm and length 8 m changed by less than 0.1% as the number of control volumes was doubled in either the x or y directions. Typically, at each axial station, 20 and 80 control volumes were used in the liquid and mixture regions, respectively, and 200 stations were used along the channel.

4. Results and discussion

Results are presented for a wide variety of conditions for condensation from a steam–air mixture, which is a commonly encountered combination of vapour and heavier non-condensing gas. Once the vapour–gas combination is selected, the functional variation of the saturation pressure-temperature relationship and all required thermal and transport properties of the vapour, the liquid, and the gas are also specified. The remaining independent parameters are the inlet conditions, the lower plate temperature, the plate spacing, the gravitational acceleration, and the angle of declination. These quantities can be varied through the following set of parameters: Re_{in}, Fr, W_{in}, ΔT, and P_{in}. For a fixed Re_{in}, Fr represents different combinations of values of H, g, and θ. If the g and H values are then also fixed, Fr represents the angle of declination; Fr tends toward infinity for the horizontal orientation, and Fr goes to zero for the vertical orientation.

The results are presented in terms of dimensionless quantities. Sample results showing detailed distributions of axial velocity, temperature, and gas mass fraction are presented to gain insight into the various transport processes involved. Special attention is given to the influences of the independent parameters on the axial distributions of film thickness and local Nusselt number.

Fig. 2 presents samples of dimensionless profiles of the axial velocity, the temperature, and the gas mass fraction across the channel at various axial locations for two values of Fr for $Re_{\mathrm{in}} = 2000$, $\Delta T = 20$ K, $W_{\mathrm{in}} = 0.10$, and $P_{\mathrm{in}} = 1$ atm. The axial velocity profiles are plotted in Fig. 2(a) with the lower

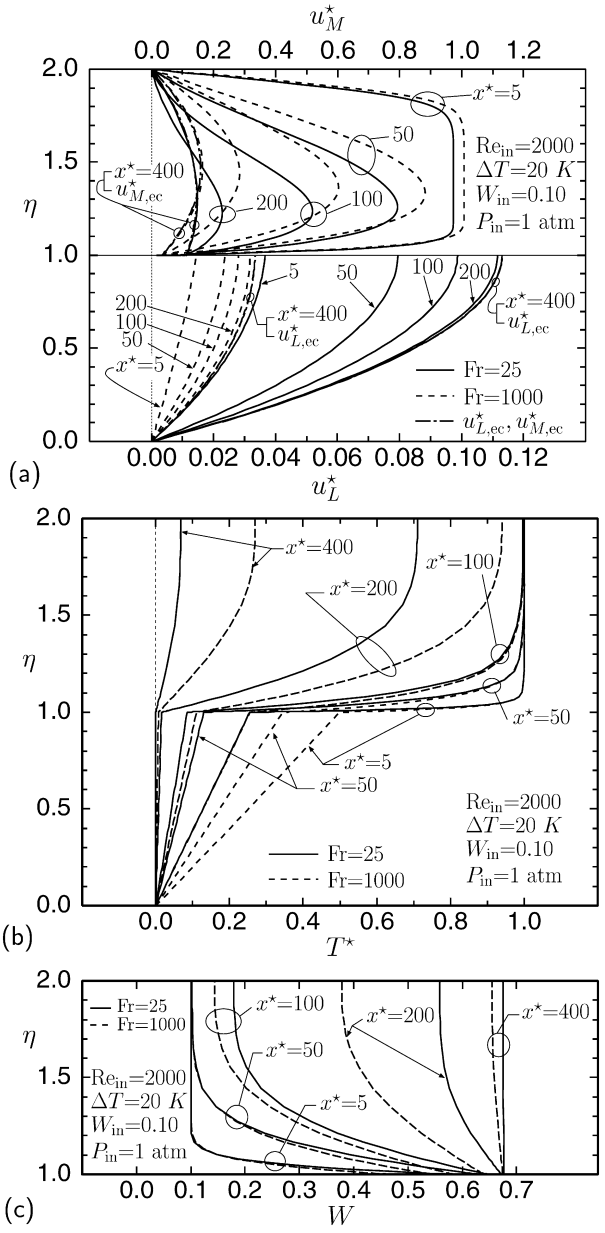

Fig. 2. Local distributions of (a) axial velocity, (b) temperature, and (c) air mass fraction at various axial locations for Froude numbers of 25 and 1000 for the case: $Re_{\mathrm{in}} = 2000$, $\Delta T = 20$ K, $W_{\mathrm{in}} = 0.10$, and $P_{\mathrm{in}} = 1$ atm.

part of the graph showing the liquid film region ($0 \leqslant \eta \leqslant 1$), and the upper part of the graph showing the mixture region ($1 \leqslant \eta \leqslant 2$). A different scale is used for the film region to enable a clearer view of the smaller film velocities. The axial trends are the same for both Froude numbers: the growing film accelerates along the channel (with increasing $x^\star$), while the mixture region velocity decreases due to mass removal. The results for $Fr = 1000$, which corresponds to a relatively small angle of declination, show a slower moving film compared to those for $Fr = 25$. It will be seen shortly in Fig. 3(a) that the faster moving film is also thinner. The analytical solution for the film velocity at the end of condensation is also plotted in Fig. 2(a), and it is observed that the $u_L^\star$ and $u_{L,\mathrm{ec}}^\star$ profiles are virtually identical at $x^\star = 400$ for both values of Fr. In the mixture region, the velocity is uniformly $u^\star = 1$ at the inlet, and the profiles at $x^\star = 5$ show that boundary layers form at the liquid–mixture interface ($\eta = 1$) and the upper plate ($\eta = 2$). At $x^\star = 400$, there are slight deviations between the $u_M^\star$ and $u_{M,\mathrm{ec}}^\star$ profiles, indicating that for this case the flow in the mixture region is not yet at the end of condensation condition at that axial distance. At a larger axial distance, the mixture region results do approach closely the analytical solution.

The dimensionless temperature profiles plotted in Fig. 2(b) show a nearly linear temperature variation in the liquid and the reduction of the temperature in both phases toward zero (corresponding to $T = T_{\mathrm{wall}}$) at large $x^\star$ for both Fr values. Under the conditions shown, however, the mixture temperature has not reached end of condensation conditions at $x^\star = 400$ for both Froude numbers. It is important to note that the interface temperature is reduced more quickly with $x^\star$ for the $Fr = 25$ case compared to the $Fr = 1000$ case. This reduction is evident in Fig. 2(b) because the liquid temperature profiles are nearly identical for $Fr = 25$ at $x^\star = 100$ and $Fr = 1000$ at $x^\star = 5$. In addition, at $x^\star = 50$ the values of $T^\star$ at $\eta = 1$ are 0.13 and 0.34 for $Fr = 25$ and $Fr = 1000$, respectively. This difference in temperatures has an impact on the local Nusselt numbers and is consistent with the interface mass fraction values discussed next.

The W profiles in Fig. 2(c) show the axial build up of gas for both Fr values. The build up of gas occurs first at the interface due to the high vapour mass flux toward the interface driven by the strong condensation rate near the inlet. The results for $Fr = 25$ show a more rapid increase of W_i along the channel than that for $Fr = 1000$. At $x^\star = 50$, the values of W_i are 0.63 and 0.55 for $Fr = 25$ and $Fr = 1000$, respectively. This difference in W_i is consistent with the temperature differences observed in Fig. 2(b). The axial increase in W and a reduction in the gradient at the interface continue in the mixture region for both Froude numbers as the profiles approach a constant value across the whole mixture region at large $x^\star$. It is observed that, at $x^\star = 400$, the W profile for $Fr = 25$ is closer to the end of condensation condition; in this case, the value of W_{ec} is 0.677 for both values of Fr.

Fig. 3 presents the axial variation of dimensionless film thickness and both local and average Nusselt numbers for the same case as in Fig. 2. The film is thinner for $Fr = 25$ compared to $Fr = 1000$, as seen in Fig. 3(a). Thus, with all other parameters fixed, a greater angle of declination produces a thinner, faster moving film. In this case, $\delta_{\mathrm{ec}}^\star$ is 0.007143 and 0.02431 for $Fr = 25$ and $Fr = 1000$, respectively. The numerical results plotted at $x^\star = 400$ in Fig. 3(a) are within 0.011% or less of their corresponding $\delta_{\mathrm{ec}}^\star$ values. This is consistent with Fig. 2(a) results which indicated that, in both cases, the film velocity field had reached end of condensation conditions at $x^\star = 400$. The results plotted in Fig. 3(b) show the expected axial decrease in Nusselt number, with the highest condensation rate near the inlet. It is interesting to note that the local and average Nusselt numbers for $Fr = 25$ are slightly greater than those for $Fr = 1000$. There is, however, not as great a difference in local Nusselt number as the film thickness (shown in Fig. 3(a)) might indicate. For example, at $x^\star = 50$, the film thickness for $Fr = 1000$ is roughly three times larger than that for $Fr = 25$. For a nearly linear film temperature profile, this would seem to indicate a local Nusselt number three times higher for $Fr = 25$. This is not so because of the much lower interface temperature for $Fr = 25$, as described with regard to Fig. 2(b). For $Fr = 25$, there is a smaller temperature difference across a thinner film, and at $x^\star = 50$, Nu_x is only 14% higher for the thinner film.

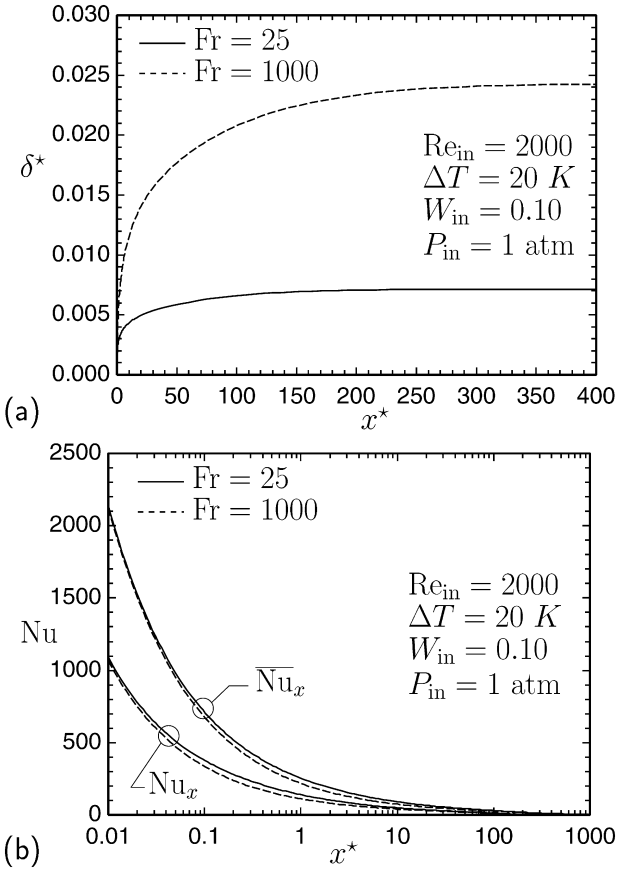

Fig. 3. Axial distributions of (a) dimensionless film thickness, and (b) local and average Nusselt numbers for Froude numbers of 25 and 1000 for the case: $Re_{\mathrm{in}} = 2000$, $\Delta T = 20$ K, $W_{\mathrm{in}} = 0.10$, and $P_{\mathrm{in}} = 1$ atm.

The graphs in Fig. 4 use the axial variation of the film thickness and the local Nusselt number to examine the effect of changing Fr for $Re_{\mathrm{in}} = 1000$, $\Delta T = 20$ K, $W_{\mathrm{in}} = 0.20$, and $P_{\mathrm{in}} = 1$ atm. These results confirm the trends that were seen

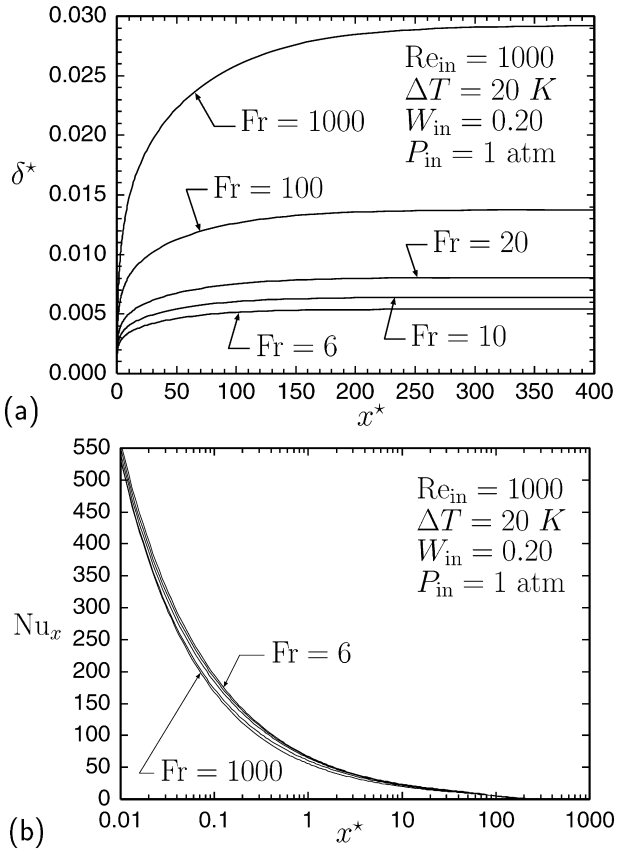

Fig. 4. Axial distributions of (a) dimensionless film thickness, and (b) local Nusselt number for various Froude numbers for the case: $Re_{in} = 1000$, $\Delta T = 20$ K, $W_{in} = 0.20$, and $P_{in} = 1$ atm.

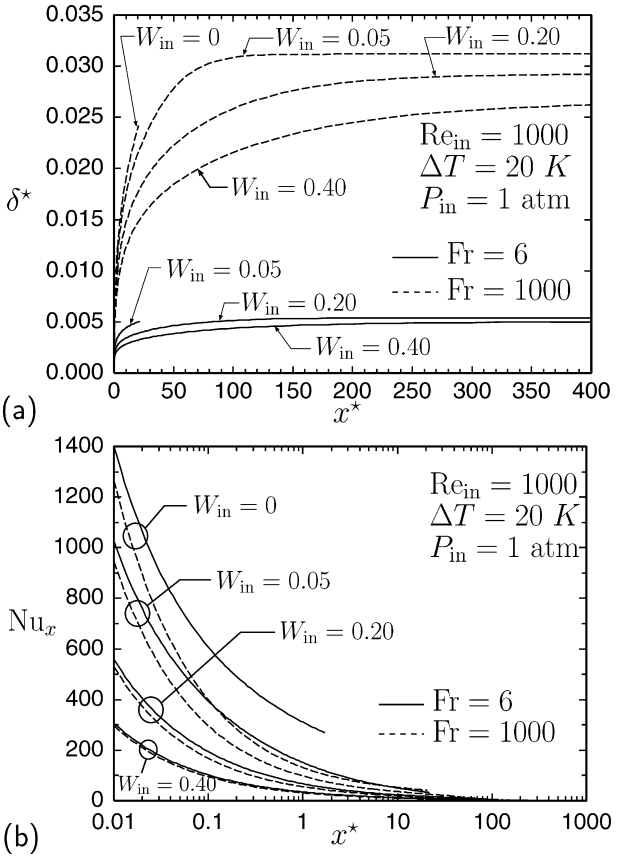

Fig. 5. Axial distributions of (a) dimensionless film thickness, and (b) local Nusselt number for Fr numbers of 6 and 1000 and various inlet air mass fractions for the case: $Re_{in} = 1000$, $\Delta T = 20$ K, and $P_{in} = 1$ atm.

in Fig. 3. In Fig. 4(a), the results also show that, when starting from a near-horizontal orientation, there is a significant reduction in the film thickness for a small increase in the angle of declination. The rate of reduction of film thickness with increased angle is smaller for higher angles (smaller Fr). The local Nusselt number trend seen in Fig. 4(b) is consistent with that discussed for Fig. 3(b): there is not a large change in Nu_x with Fr under the conditions used.

The graphs in Fig. 5 use the axial variation of the film thickness and the local Nusselt number to examine the effect of changing W_{in} for the same Re_{in}, ΔT, and P_{in} as in Fig. 4 for two values of Fr. The curves in Fig. 5(a) show the same trend for both Froude numbers: the film thickness is reduced as W_{in} is increased. This trend is consistent with the well-known detrimental effect on heat transfer of increasing amounts of non-condensing gas. For pure vapour, the condensation rate is highest, resulting in reverse flow for both Fr values. For the conditions given in Fig. 5(a), reverse flow was also encountered at $W_{in} = 0.05$ for $Fr = 25$. The film is again thicker for higher Fr, and the effect on the film thickness of increasing W_{in} is more pronounced for $Fr = 1000$.

In terms of local heat transfer, shown in Fig. 5(b), Nu_x is reduced as W_{in} is increased even though the film is thinner. This is due to the reduction of the interface temperature with an increase in W_i. It is also observed that the local Nusselt number is always larger for lower Fr for a given value of W_{in}. As the gas mass fraction is reduced, Nu_x becomes relatively greater for $Fr = 6$ compared to $Fr = 1000$, but still not equivalent to the ratio of film thicknesses.

The graphs in Figs. 6 and 7 present the effects of changing ΔT on axial variations of $\delta^\star$ and Nu_x for $Fr = 6$ and $Fr = 1000$, respectively, for $Re_{in} = 1000$ and $P_{in} = 1$ atm and two values of W_{in}. The results in Fig. 6(a) show that film thickness increases with ΔT, corresponding to increasing condensation rate. In the case of the lower W_{in}, reverse flow was encountered at $\Delta T = 20$ K and $\Delta T = 40$ K. At $W_{in} = 0.40$, the condensation rate is lower, the film is thinner, and no reverse flow occurs. In Fig. 6(b), the results show that Nu_x is reduced as W_{in} is increased, and Nu_x decreases with increased ΔT. This trend occurs because the increase in q''_{wall} with ΔT occurs at a slower rate than the increase in ΔT itself.

The trends of the results presented in Fig. 7 are very similar to those in Fig. 6. The change to $Fr = 1000$ produced a thicker film and lower Nu_x, and no reverse flow was encountered under the conditions used.

Fig. 8 presents graphs of film thickness and local Nusselt number for three values of Re_{in} and two Froude numbers for $\Delta T = 20$ K, $W_{in} = 0.20$, and $P_{in} = 1$ atm. Fig. 8(a) shows thinner films with increased Re_{in} because of the greater shear force at the interface. As expected, Nu_x increases with Re_{in}, due to the decrease in film thickness, as depicted in Fig. 8(b).

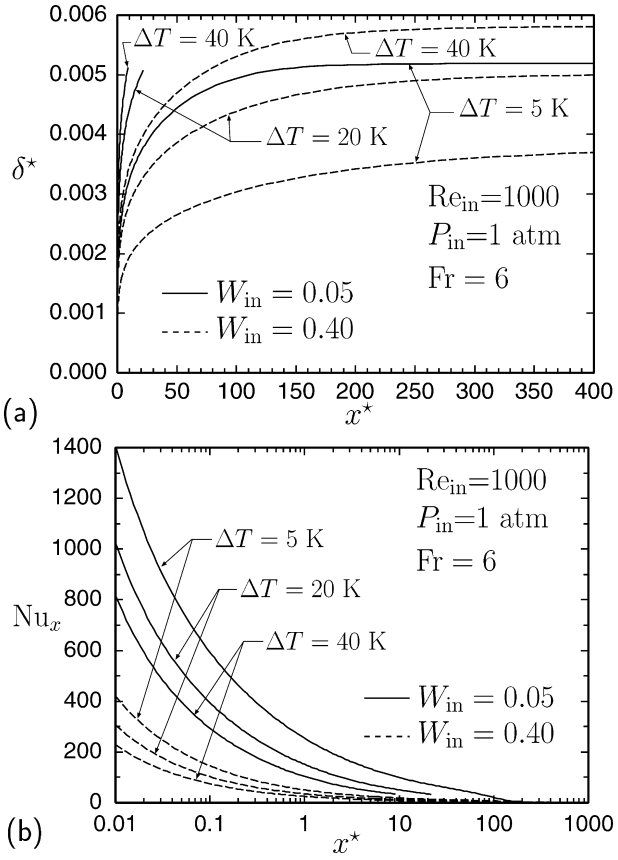

Fig. 6. Axial distributions of (a) dimensionless film thickness, and (b) local Nusselt number for two inlet air mass fractions and various ΔT values for the case: $Fr = 6$, $Re_{in} = 1000$, and $P_{in} = 1$ atm.

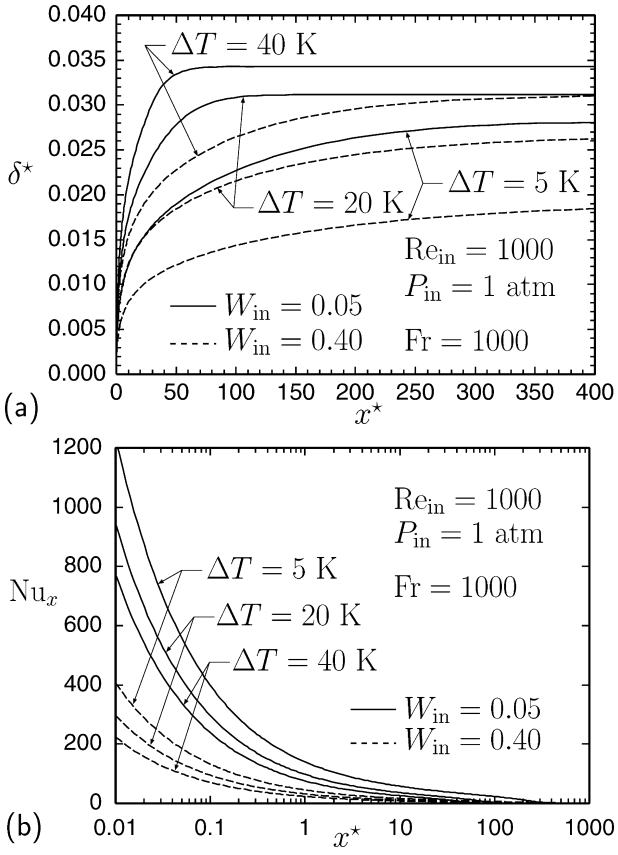

Fig. 7. Axial distributions of (a) dimensionless film thickness, and (b) local Nusselt number for two inlet air mass fractions and various ΔT values for the case: $Fr = 1000$, $Re_{in} = 1000$, and $P_{in} = 1$ atm.

Other computations were performed in which the inlet pressure was varied [14]. In these tests, P_{in} was varied from 0.5 to 2.0 atm, and the key effect demonstrated in the results was the effect of changes in fluid properties. Overall, an increase in P_{in} produced an increase in film thickness and a decrease in Nu_x. The overall change in Nu_x over the four-fold increase in P_{in} was not substantial. The overall change in Nu_x for $x^\star \leqslant 100$ for $Fr = 6$ and $Fr = 1000$ was less than 17% and 15%, respectively. At higher $x^\star$, the overall differences are small, and so is Nu_x.

5. Summary and conclusions

A finite-control-volume method is utilized to solve the complete set of two-phase boundary layer equations for laminar film condensation in the presence of a noncondensable gas. Computations were made for declining parallel-plate channels with a cooled lower wall and an insulated upper wall. A fully coupled marching solution scheme was employed to produce detailed profiles of velocity, temperature, and gas mass fraction, as well as axial distributions of local film thickness and Nusselt number. Results for steam–air mixtures are presented and the effects of changes in Froude number, inlet gas mass fraction, inlet Reynolds number, and inlet temperature difference are examined. For all other parameters being fixed, variation of the Froude number corresponds to changing the angle of declination.

It was found that a decrease in Fr (increase in angle of declination) resulted in thinner, faster moving liquid films. The thinner films did not show a substantial increase in local Nusselt number, however, due to a decrease in the temperature difference across the film. An increase in W_{in} resulted in a decrease in film thickness and, when coupled with a corresponding decrease in the interface temperature, a decrease in the local Nusselt number as well. An increase in ΔT resulted in an increase in film thickness and a decrease in Nu_x because the wall heat flux did not increase as fast as the inlet temperature difference. Increasing Re_{in} always produced thinner films and higher Nu_x. The effect on the film thickness of changing Re_{in} was more pronounced at higher Fr.

Acknowledgements

The support for this project from the Natural Sciences and Engineering Research Council of Canada (NSERC) is gratefully acknowledged.

Appendix A. End of condensation analytical solution

The focus of this analysis is on a region down the channel (shown in Fig. 1) after evolution of the flow to the condition where there is no further heat transfer because the temperatures in both phases are uniform at T_{wall} and constant with respect

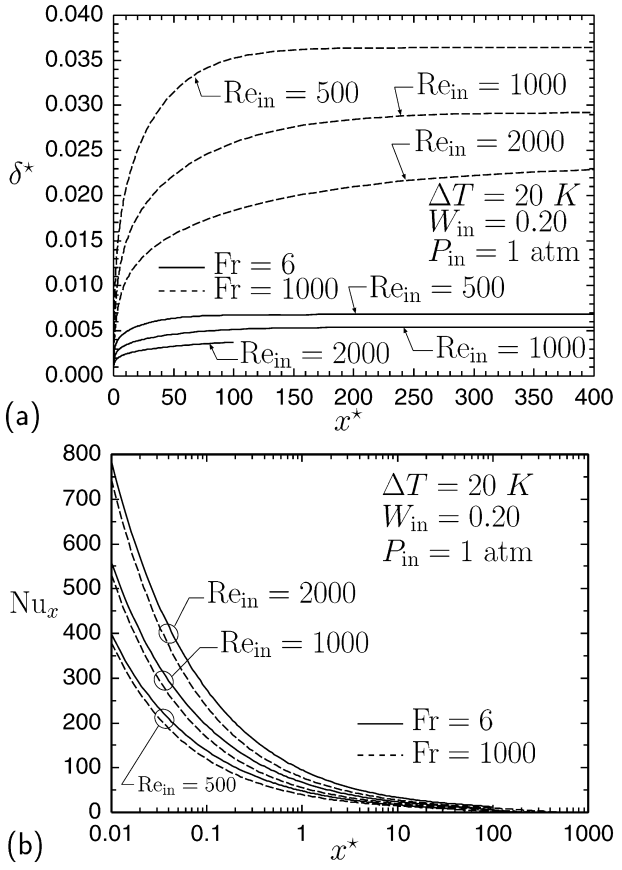

Fig. 8. Axial distributions of (a) dimensionless film thickness, and (b) local Nusselt number for Froude numbers of 6 and 1000 and various inlet Reynolds numbers for the case: $\Delta T = 20$ K, $W_{\text{in}} = 0.20$, and $P_{\text{in}} = 1$ atm.

to x. The mixture then consists of a gas fully saturated with vapour with a uniform gas concentration W_{ec}, which can be easily calculated using standard thermodynamic relations [17]. At this end of condensation condition, the axial velocities, gas concentration, film thickness, and pressure gradient are also independent of x. The density and viscosity of the liquid film and the mixture at the end of condensation are simply denoted ρ_L and μ_L and ρ_M and μ_M, respectively.

When the flow is independent of x, the simplified momentum equations for the liquid and mixture regions, in dimensionless form, are:

$$\frac{\mathrm{d}^2 u^\star_{L,\text{ec}}}{\mathrm{d}y^{\star 2}} = \left(\frac{\mu_{\text{in}}}{\mu_L}\right) Re_{\text{in}} K^\star_L \tag{21}$$

and

$$\frac{\mathrm{d}^2 u^\star_{M,\text{ec}}}{\mathrm{d}y^{\star 2}} = \left(\frac{\mu_{\text{in}}}{\mu_M}\right) Re_{\text{in}} K^\star_M \tag{22}$$

where

$$K^\star_L = \left[\frac{1}{2}\left(\frac{\mathrm{d}P^\star}{\mathrm{d}x^\star}\right)_{\text{ec}} - \left(\frac{\rho_L}{\rho_{\text{in}}}\right)\frac{1}{Fr}\right] \tag{23}$$

and

$$K^\star_M = \left[\frac{1}{2}\left(\frac{\mathrm{d}P^\star}{\mathrm{d}x^\star}\right)_{\text{ec}} - \left(\frac{\rho_M}{\rho_{\text{in}}}\right)\frac{1}{Fr}\right] \tag{24}$$

The boundary conditions for Eqs. (21) and (22) are zero velocity at both plates and equal velocity and shear stress at the liquid–mixture interface. Integrating Eqs. (21) and (22) and applying the boundary conditions yields the following velocity distributions:

$$u^\star_{L,\text{ec}} = \frac{1}{2}\left(\frac{\mu_{\text{in}}}{\mu_L}\right) Re_{\text{in}} K^\star_L \left(y^{\star 2} + C_1\, y^\star\right) \tag{25}$$

and

$$u^\star_{M,\text{ec}} = \frac{1}{2}\left(\frac{\mu_{\text{in}}}{\mu_M}\right) Re_{\text{in}} K^\star_M \left\{ y^{\star 2} + \left[2\left(\frac{K^\star_L}{K^\star_M} - 1\right)\delta^\star_{\text{ec}} + \frac{K^\star_L}{K^\star_M} C_1\right](y^\star - 1) - 1\right\} \tag{26}$$

where

$$C_1 = \frac{\{[2 - (\frac{K^\star_M}{K^\star_L} + \frac{\mu_M}{\mu_L})]\delta^{\star\,2}_{\text{ec}} - 2[1 - \frac{K^\star_M}{K^\star_L}]\delta^\star_{\text{ec}} - \frac{K^\star_M}{K^\star_L}\}}{[1 + (\frac{\mu_M}{\mu_L} - 1)\delta^\star_{\text{ec}}]} \tag{27}$$

Simple mass balances can be performed on both the liquid and mixture mass flows, and can be written in dimensionless form as:

$$\int_0^{\delta^\star_{\text{ec}}} u^\star_{L,\text{ec}}\, \mathrm{d}y^\star = \left(\frac{\rho_{\text{in}}}{\rho_L}\right)\left(1 - \frac{W_{\text{in}}}{W_{\text{ec}}}\right) \tag{28}$$

and

$$\int_{\delta^\star_{\text{ec}}}^{1} u^\star_{M,\text{ec}}\, \mathrm{d}y^\star = \left(\frac{\rho_{\text{in}}}{\rho_M}\right)\frac{W_{\text{in}}}{W_{\text{ec}}} \tag{29}$$

Substituting from Eq. (25) into Eq. (28) and from Eq. (26) into Eq. (29), produces two equations that can be written as:

$$\left(\frac{\mathrm{d}P^\star}{\mathrm{d}x^\star}\right)_{\text{ec}} = \frac{(a_0 + a_1\delta^\star_{\text{ec}} + b_2\delta^{\star\,2}_{\text{ec}} + b_3\delta^{\star\,3}_{\text{ec}} + b_4\delta^{\star\,4}_{\text{ec}})}{(d_2\delta^{\star\,2}_{\text{ec}} + d_3\delta^{\star\,3}_{\text{ec}} + d_4\delta^{\star\,4}_{\text{ec}})} \tag{30}$$

and

$$\left(\frac{\mathrm{d}P^\star}{\mathrm{d}x^\star}\right)_{\text{ec}} = \frac{(e_0 + e_1\delta^\star_{\text{ec}} + f_0 + f_1\delta^\star_{\text{ec}} + f_2\delta^{\star\,2}_{\text{ec}} + f_3\delta^{\star\,3}_{\text{ec}} + f_4\delta^{\star\,4}_{\text{ec}})}{(g_0 + g_1\delta^\star_{\text{ec}} + g_2\delta^{\star\,2}_{\text{ec}} + g_3\delta^{\star\,3}_{\text{ec}} + g_4\delta^{\star\,4}_{\text{ec}})} \tag{31}$$

The coefficients in Eqs. (30) and (31) are given in Table 1. The nomenclature of the coefficients for Eqs. (30) and (31) was established so that the b and f coefficients go to zero in the horizontal orientation (when $1/Fr \to 0$). In this limit, only the a, e, d, and g coefficients remain, and the solution presented here can be shown to be the same as that presented for end of condensation in [4].

Equating the pressure gradient in Eqs. (30) and (31) produces an eighth order polynomial which can be solved for the value of $\delta^\star_{\text{ec}}$. This is the value of the dimensionless film thickness at the end of condensation for a given set of values for ρ_{in}, ρ_L, ρ_M, μ_{in}, μ_L, μ_M, Re_{in}, Fr, W_{in}, and W_{ec}. The value of $\delta^\star_{\text{ec}}$ is then substituted into either Equation (30) or (31) to determine $(\mathrm{d}P^\star/\mathrm{d}x^\star)_{\text{ec}}$. Once the values of $\delta^\star_{\text{ec}}$ and $(\mathrm{d}P^\star/\mathrm{d}x^\star)_{\text{ec}}$ are

Table 1
Coefficients of equations for dimensionless pressure gradient (Eqs. (30) and (31))

Coefficients of Eq. (30)	Coefficients of Eq. (31)
$a_0 = \frac{24}{Re_{\text{in}}}\frac{\rho_{\text{in}}}{\rho_L}\frac{\mu_L}{\mu_{\text{in}}}\left(1-\frac{W_{\text{in}}}{W_{\text{ec}}}\right)$	$e_0 = \frac{24}{Re_{\text{in}}}\frac{\rho_{\text{in}}}{\rho_M}\frac{\mu_M}{\mu_{\text{in}}}\frac{W_{\text{in}}}{W_{\text{ec}}}$
$a_1 = a_0\left(\frac{\mu_M}{\mu_L}-1\right)$	$e_1 = e_0\left(\frac{\mu_M}{\mu_L}-1\right)$
$b_2 = -\frac{\rho_M}{\rho_{\text{in}}}\frac{6}{Fr}$	$f_0 = -\frac{\rho_M}{\rho_{\text{in}}}\frac{2}{Fr}$
$b_3 = -\frac{\rho_L}{\rho_{\text{in}}}\frac{8}{Fr}+\frac{\rho_M}{\rho_{\text{in}}}\frac{12}{Fr}$	$f_1 = \frac{\rho_M}{\rho_{\text{in}}}\frac{8}{Fr}\left(1-\frac{\mu_M}{\mu_L}\right)$
$b_4 = \frac{\rho_L}{\rho_{\text{in}}}\frac{2}{Fr}\left(4-\frac{\mu_M}{\mu_L}\right)-\frac{\rho_M}{\rho_{\text{in}}}\frac{6}{Fr}$	$f_2 = \frac{\rho_M}{\rho_{\text{in}}}\frac{12}{Fr}\left(2\frac{\mu_M}{\mu_L}-1\right)-\frac{\rho_L}{\rho_{\text{in}}}\frac{6}{Fr}\frac{\mu_M}{\mu_L}$
$d_2 = -3$	$f_3 = \frac{\rho_M}{\rho_{\text{in}}}\frac{8}{Fr}\left(1-3\frac{\mu_M}{\mu_L}\right)+\frac{\rho_L}{\rho_{\text{in}}}\frac{12}{Fr}\frac{\mu_M}{\mu_L}$
$d_3 = 2$	$f_4 = \frac{\rho_M}{\rho_{\text{in}}}\frac{2}{Fr}\left(4\frac{\mu_M}{\mu_L}-1\right)-\frac{\rho_L}{\rho_{\text{in}}}\frac{6}{Fr}\frac{\mu_M}{\mu_L}$
$d_4 = \left(1-\frac{\mu_M}{\mu_L}\right)$	$g_0 = -1$
	$g_1 = 4\left(1-\frac{\mu_M}{\mu_L}\right)$
	$g_2 = 3\left(3\frac{\mu_M}{\mu_L}-2\right)$
	$g_3 = 2\left(2-3\frac{\mu_M}{\mu_L}\right)$
	$g_4 = \left(\frac{\mu_M}{\mu_L}-1\right)$

known, the coefficients required to determine $u^{\star}_{L,\text{ec}}$ and $u^{\star}_{M,\text{ec}}$ (from Eqs. (25) and (26)) are easily determined.

References

[1] H. Louahlia, P.K. Panday, Étude de la condensation par convection forcée du R113, R152a et du R12 sur une plaque plane horizontale, J. Phys. III 6 (7) (1996) 873–892.

[2] H. Louahlia, P.K. Panday, Transfert thermique pour la condensation du R123, du R134a et de leurs mélanges, en écoulement forcé entre deux plaques planes horizontales. Étude numérique, Rev. Gen. Therm. 35 (417) (1996) 615–624.

[3] A. Narain, Y. Kizilyalli, Pressure driven flow of pure vapor undergoing laminar-film condensation between parallel plates, Int. J. Nonlinear. Mech. 26 (5) (1991) 501–520.

[4] E.C. Siow, S.J. Ormiston, H.M. Soliman, Fully-coupled solution of a two-phase model for laminar film condensation of vapor–gas mixtures in horizontal channels, Int. J. Heat Mass Transfer 45 (18) (2002) 3689–3702.

[5] H. Louahlia, P.K. Panday, Condensation en film entre deux plaques planes verticales: Comparaison des performances thermiques du R134a et du R12, Canad. J. Chem. Eng. 75 (4) (1997) 704–711.

[6] P.K. Panday, Two-dimensional turbulent film condensation of vapours flowing inside a vertical tube and between parallel plates: A numerical approach, Int. J. Refrig. 26 (4) (2003) 492–503.

[7] E.C. Siow, S.J. Ormiston, H.M. Soliman, A two-phase model for laminar film condensation from steam–air mixtures in vertical parallel-plate channels, Heat Mass Transfer 40 (5) (2004) 365–375.

[8] A. Narain, G. Yu, Q. Liu, Interfacial shear models and their required asymptotic form for annular/stratified film condensation flows in inclined channels and vertical pipes, Int. J. Heat Mass Transfer 40 (15) (1997) 3559–3575.

[9] E.C. Siow, S.J. Ormiston, H.M. Soliman, Laminar film condensation from vapor–gas mixtures in downward-inclined parallel-plate channels, in: Proceedings of the 12th International Heat Transfer Conference, Grenoble, France, 2002, vol. 3, pp. 905–910.

[10] Q. Lu, N.V. Suryanarayana, Condensation of a vapor flowing inside a horizontal rectangular duct, J. Heat Transfer 117 (2) (1995) 418–424.

[11] W. Yu, S.U.S. Choi, D.M. France, M.W. Wambsganss, Single-sided steam condensing inside a rectangular horizontal channel, Int. J. Heat Mass Transfer 45 (18) (2002) 3715–3724.

[12] B.J. Chung, S. Kim, M.C. Kim, Film condensations of flowing mixtures of steam and air on an inclined flat plate, Int. Commun. Heat Mass 32 (1–2) (2005) 233–239.

[13] V. Srzic, H.M. Soliman, S.J. Ormiston, Analysis of laminar mixed-convection condensation on isothermal plates using the full boundary-layer equations: Mixtures of a vapor and a lighter gas, Int. J. Heat Mass Transfer 42 (4) (1999) 685–695.

[14] E.C. Siow, Numerical solution of a two-phase model for laminar film condensation of vapour–gas mixtures in channels, M.Sc. thesis, University of Manitoba, Canada, 2001.

[15] S.V. Patankar, Numerical Heat Transfer and Fluid Flow, Hemisphere, Washington, 1980.

[16] Y.S. Chin, S.J. Ormiston, H.M. Soliman, A two-phase boundary-layer model for laminar mixed-convection condensation with a noncondensable gas on inclined plates, Heat Mass Transfer 34 (4) (1998) 271–277.

[17] R.E. Sonntag, C. Borgnakke, G.J. Van Wylen, Fundamentals of Thermodynamics, sixth ed., Wiley, New York, 2003.